Astronomy & Astrophysics manuscript no. main
March 14, 2025
© ESO 2025

arXiv:2412.13250v2 [astro-ph.GA] 13 Mar 2025

Cosmology with Supernova Encore in the lensing cluster MACS J0138−2155 – Spectroscopy with MUSE

G. Granata[1,2,3], G. B. Caminha[4,5], S. Ertl[4,5], C. Grillo[1,6], S. Schuldt[1,6], S. H. Suyu[5,4], A. Acebron[7], P. Bergamini[1,8], R. Cañameras[9], P. Rosati[2,8], and S. Taubenberger[4,5]

[1] Dipartimento di Fisica, Università degli Studi di Milano, via Celoria 16, 20133 Milano, Italy
[2] Dipartimento di Fisica e Scienze della Terra, Università degli Studi di Ferrara, via Saragat 1, 44122 Ferrara, Italy
[3] Institute of Cosmology and Gravitation, University of Portsmouth, Burnaby Rd, Portsmouth PO1 3FX, UK
e-mail: giovanni.granata@port.ac.uk
[4] Max-Planck-Institut für Astrophysik, Karl-Schwarzschild Straße 1, 85748 Garching, Germany
[5] Technical University of Munich, TUM School of Natural Sciences, Physics Department, James-Franck-Straße 1, 85748 Garching, Germany
[6] INAF – IASF Milano, via Corti 12, 20133 Milano, Italy
[7] Instituto de Física de Cantabria (CSIC-UC), Avda. Los Castros s/n, 39005 Santander, Spain
[8] INAF – OAS, Osservatorio di Astrofisica e Scienza dello Spazio di Bologna, via Gobetti 93/3, 40129 Bologna, Italy
[9] Aix Marseille Univ, CNRS, CNES, LAM, Marseille, France

Received 17 Dec 2024; accepted 10 Feb 2025

ABSTRACT

We present a comprehensive spectroscopic analysis of MACS J0138−2155, at $z = 0.336$, the first galaxy cluster hosting two strongly-lensed supernovae (SNe), Requiem and Encore, providing us with a chance to obtain a reliable H_0 measurement from the time delays between the multiple images. We take advantage of new spectroscopic data from the Multi Unit Spectroscopic Explorer (MUSE) on the Very Large Telescope, complemented with archival imaging from the *Hubble* Space Telescope. The MUSE data cover a central 1 arcmin^2 of the lensing cluster, for a total depth of 3.7 hours, including 2.9 hours recently obtained by our Target of Opportunity programme. Based on these observations, we release a new spectroscopic catalogue containing reliable redshifts for 107 objects. This includes 50 galaxy cluster members with secure redshift values in the range $0.324 < z < 0.349$, and 13 lensed multiple images from four background sources between $0.767 \leq z \leq 3.420$, including four images of the host galaxy of the two SNe. We exploit the MUSE data to study the stellar kinematics of 14 bright cluster members and two background galaxies, obtaining reliable measurements of their line-of-sight velocity dispersion. Finally, we combine these results with measurements of the total magnitude of the cluster members in the *Hubble* Space Telescope F160W band to calibrate the Faber-Jackson relation between luminosity and stellar velocity dispersion ($L \propto \sigma_v^{1/\alpha}$) for the early-type cluster member galaxies, measuring a slope $\alpha = 0.25^{+0.05}_{-0.05}$, and a scatter of 25^{+6}_{-4} km s^{-1} about the relation. We compare the calibrated relation with six other strong lensing clusters in the redshift range $0.31 \leq z \leq 0.59$, finding a general agreement and no clear sign of evolution with redshift. A pure and complete sample of cluster member galaxies and a reliable characterisation of their total mass structure are key to building accurate total mass maps of the cluster, mitigating the impact of parametric degeneracies, which is necessary for inferring the value of H_0 from the measured time delays between the lensed images of the two SNe.

Key words. galaxies: clusters: individual (MACS J0138.0−2155) – gravitational lensing: strong – galaxies: distances and redshifts – galaxies: kinematics and dynamics – galaxies: elliptical and lenticular, cD

1. Introduction

Strong gravitational lensing (SL) by galaxy clusters has recently emerged as a unique bridge between astrophysics and cosmology. Galaxy clusters are remarkable as the most massive gravitationally bound structures in the Universe, with a mass budget dominated by dark matter (DM). Strong gravitational lensing is the most accurate probe of the total mass in the cores of massive clusters; when combined with tracers of the baryonic mass, it allows us to disentangle the mass distribution of the DM haloes (e.g. Natarajan & Kneib 1997; Caminha et al. 2019; Granata et al. 2022). As such, SL models of galaxy clusters have been instrumental in unveiling and tackling some crucial open problems in state-of-the-art cosmology (e.g. Grillo et al. 2015, 2018; Meneghetti et al. 2020).

Galaxy clusters are privileged tracers of the formation and evolution of massive structures from the primordial density fluctuations through hierarchical mergers. While N-body simulations predict a universal Navarro-Frenk-White (NFW) mass profile (Navarro et al. 1997), baryonic physics and its interplay with DM play a fundamental role in re-sculpting DM haloes. Recent comparisons between SL models of massive galaxy clusters and high-resolution cosmological hydrodynamical simulations showed that the latter cannot reproduce the observed galaxy-galaxy SL cross section (Meneghetti et al. 2020, 2022, 2023), as they predict galaxy cluster sub-haloes to be less compact than found in SL models (Ragagnin et al. 2022). Improvements of our SL modelling techniques can test this discrepancy, which has the potential to shed light on the complex baryon-DM interplay that affects galaxy formation and evolution in clusters and potentially uncover issues in their current description within the Λ cold dark matter (ΛCDM) framework.

In addition, SL models of galaxy clusters have the potential to play a crucial role for cosmographic studies. A 5σ discrepancy between the measured values of the Hubble constant, H_0, obtained through the study of the anisotropy of the cosmic microwave background (Planck Collaboration 2020) and the Cepheid distance ladder with type Ia SNe (Riess et al. 2022) has recently emerged. The discrepancy is under debate, partly because effects such as the choice of calibrators, sample selection, and dust corrections of SNe Ia could potentially affect H_0 measurements (e.g. Efstathiou 2020; Riess et al. 2024; Freedman et al. 2024; Riess et al. 2024; Wojtak & Hjorth 2022, 2024). Independent methods to assess the discrepancy are therefore helpful (Moresco et al. 2022), since they would unveil potential systematic effects or new physics beyond the ΛCDM paradigm. Quasars and SNe lensed by galaxy clusters (or individual galaxies) are an independent (i.e. not affected by the same systematics and degeneracies) precise probe of H_0 (Refsdal 1964), which makes use of measured time delays between the multiple images of the variable background source. These are caused by the lens gravitational potential and by different length of the light paths connecting the source to the multiple images. The light curves of SNe are drastically changing, which allow for measurements of the time delays, typically on the order of weeks to years, with uncertainties within a few days (Kelly et al. 2023; Dhawan et al. 2020; Pierel et al. 2024a; Huber & Suyu 2024). The time delays depend on the exact value of the Hubble constant and on the total gravitational potential of the cluster; an accurate SL model of the total mass distribution in the cluster core is thus key to obtaining a reliable H_0 measurement from the time delays.

Improving the accuracy of our description of the total mass distribution of galaxy clusters on sub-halo scales is thus crucial, both to probe the properties of the cluster sub-structures and to measure H_0 using time-variable sources. Constraining the mass structure of the cluster members with only cluster-scale SL modelling, however, potentially leads to parametric degeneracy that hinders the reconstruction of their compactness (Granata et al. 2023). Several recent works have shown how this degeneracy can be broken by taking advantage of observations from MUSE (Bacon et al. 2012) at the Very Large Telescope (VLT). The $1\,\mathrm{arcmin}^2$ field of view (FoV) of MUSE covers the typical size of the central region of massive clusters at $z \approx 0.3$ (see Fig. 1), allowing one to securely identify cluster galaxies (e.g Mercurio et al. 2021; Lagattuta et al. 2022) and to obtain priors on the total mass distribution of the cluster members from their measured stellar kinematics (Bergamini et al. 2019; Granata et al. 2022; Beauchesne et al. 2024). Furthermore, MUSE allows us to build a complete spectroscopic catalogue that can be used for the detection of an unprecedented number of spectroscopically confirmed lensed background sources within an extended redshift range (up to $z \sim 6$) (e.g. Richard et al. 2015; Grillo et al. 2016; Jauzac et al. 2019; Bergamini et al. 2023b; Caminha et al. 2023), which provide very stringent constraints on the lens total mass distribution, and help us break the mass-sheet degeneracy affecting its reconstruction.

This work focuses on the MUSE observations of the galaxy cluster MACS J0138−2155 (hereafter MACS0138, Newman et al. 2018a,b). After the observation of the strongly-lensed SN Requiem, a likely Type Ia SN (Rodney et al. 2021), in a host galaxy at redshift $z \approx 2$, a second SN, SN Encore, suitable for time-delay cosmography, was observed in the same host galaxy (Pierel et al. 2024b). The SN was spectroscopically studied in Dhawan et al. (2024) and identified as Type Ia. In this paper, we present a new MUSE spectroscopic catalogue of MACS0138, containing 107 reliable redshift measurements, including 50 galaxy cluster members and 13 lensed images from four background sources, which is used to build a set of new, independent SL models of the galaxy cluster based on a reliable selection of the cluster members and a pure sample of multiple images. We have studied the stellar kinematics of 16 galaxies (14 cluster members and two background objects) falling within the FoV of MUSE, and calibrated the Faber-Jackson relation (Faber & Jackson 1976) for the cluster members, which is crucial to break the degeneracy between the values of the velocity dispersion and the truncaction radius affecting the total mass reconstruction of cluster members in SL models (Bergamini et al. 2019).

To get an indication of the physical scales from the observed angular scales of our system, we use a flat ΛCDM cosmology with $H_0 = 70\,\mathrm{km\,s^{-1}\,Mpc^{-1}}$, $\Omega_\mathrm{M} = 1 - \Omega_\Lambda = 0.3$, where $1''$ corresponds to a scale of 4.809 kpc at $z = 0.336$, the redshift of MACS0138. All magnitudes are expressed in the AB system.

2. MUSE observations and data reduction

The galaxy cluster MACS0138 was targeted by two MUSE programmes between 2019 and 2023. In September of 2019, the ESO programme ID 0103.A-0777 (P.I. A. Edge) obtained data covering the core of the cluster with an exposure time of approximately 49 minutes on target. Later on, in December of 2023, after the detection of SN Encore, the Target of Opportunity programme ID 110.23PS (P.I. S. H. Suyu) obtained 2.9 hours of additional data for the same region of the cluster, to increase the depth of the observations. The latter data set was obtained using the ground layer adaptive optics (GLAO) system in order to provide improved spatial resolution due to the reduced point-spread-function (PSF). The FoV of the combined MUSE observations is shown in Fig. 1. It covers the cluster core with an extension of approximately 1 arcmin across, or 289 kpc at $z = 0.336$.

We used the MUSE data-reduction pipeline version `v2.8.5` (Weilbacher et al. 2020) to process and calibrate the two data sets and combine them into one final data cube. We followed the standard procedure, such as bias subtraction, flat-fielding, wavelength calibration, and exposure map alignment. Moreover, we used the self-calibration method, implemented in the reduction pipeline, to minimise the instrumental variations across each integral field unit slice and to improve the background subtraction. We also made use of the Zurich Atmosphere Purge (ZAP, Soto et al. 2016) to remove instrumental and sky residuals not fully corrected for by the standard reduction recipes. No bright stars for a precise PSF measurement are present within the FoV of approximately $1\,\mathrm{arcmin}^2$. However, the mean seeing from the Differential Image Motion Monitor station was approximately $0.8''$ during all observations. Moreover, because of the GLAO laser guiding system of the adaptive optics mode used during the observations in December 2023, the region within the wavelength range between 5800Å and 5965Å was masked out. The final data cube consequently has a reduced effective exposure time in this specific wavelength range, which does not however affect the final spectroscopic measurements. The MUSE data cube was aligned with the *James Webb* Space Telescope (*JWST*) images from Pierel et al. (2024b), using as references the Near Infrared Camera (NIRCam) filter F115W band and the MUSE 'white image'. We degraded the *JWST* image to the MUSE white image resolution and employed the positions of approximately 50 compact sources to match both data sets.

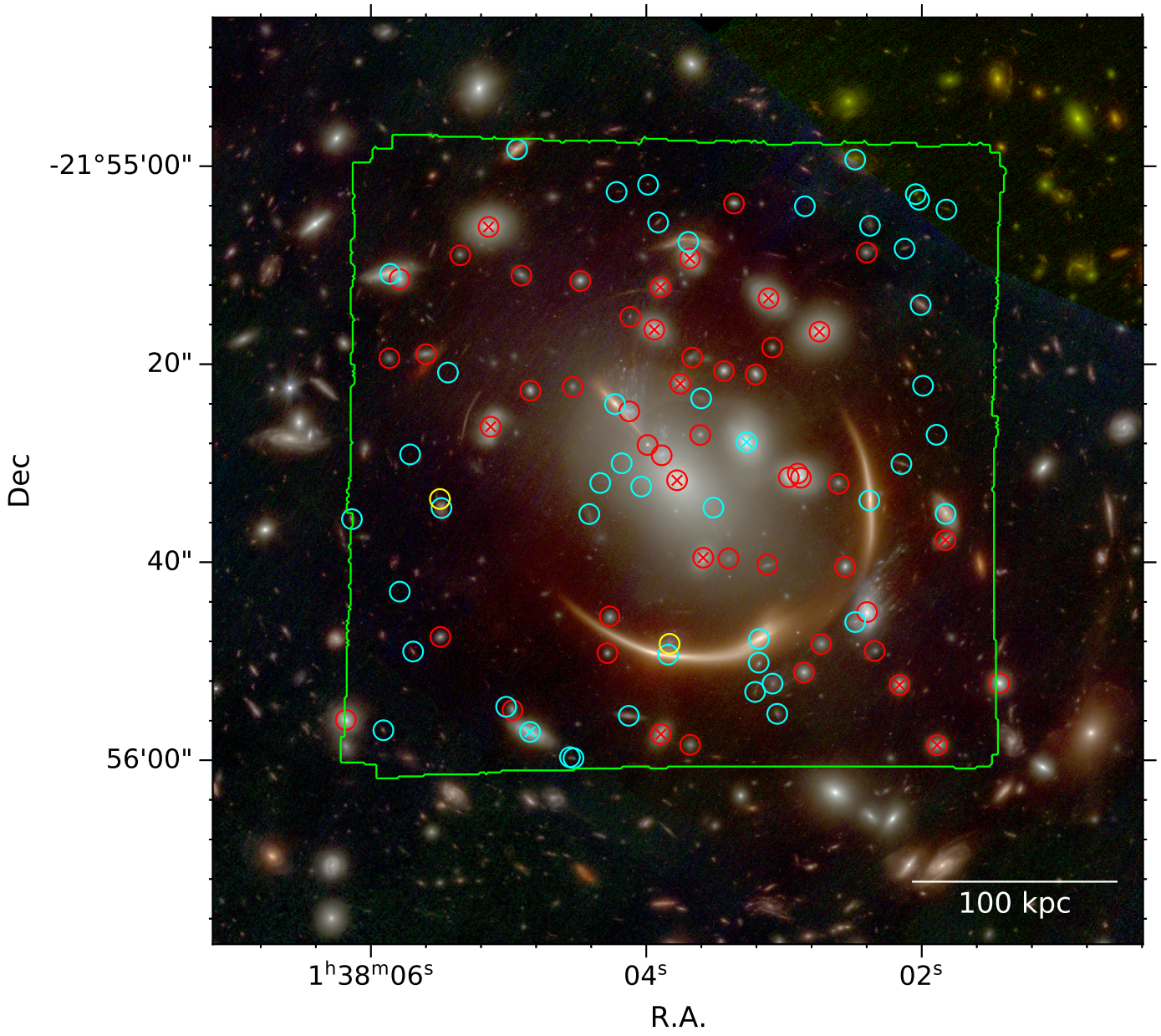


Fig. 1: MUSE FoV on MACS0138 overlaid on a colour image built from *JWST* NIRCam images (red: F277W, F356W, F444W; green: F150W, F200W; blue: F115W). The green region shows the FoV of the final MUSE data cube combining all exposures. Circles indicate spectroscopically confirmed foreground galaxies (yellow), cluster members (red) and background objects (cyan). We mark the cluster members and background galaxies for which we present a stellar velocity dispersion measurement with crosses.

3. Spectroscopic redshift measurements

In order to obtain redshift measurements for as many sources as possible, we followed the method described in Sect. 2.2 of Caminha et al. (2023). We first extracted the spectra of all *JWST* detections in order to measure their redshifts. In this step, we adopted circular apertures with a 0.8″ radius to obtain one-dimensional spectra of all objects. We carefully inspected all spectra, and in the cases with continuum detection we cross-correlated the data with templates in order to obtain precise redshift measurements. With the help of spectral template matching of different galaxies, as well as the identification of emission lines (such as [OII], Balmer lines, Lyman-α, and UV carbon lines), we built our redshift catalogue. We assigned a quality flag (QF) to each redshift measurement, following Balestra et al. (2016) and Caminha et al. (2016), which quantifies its reliability: 'insecure' (QF = 1), 'likely' (QF = 2), 'secure' (QF = 3), or 'based on a single emission line' (QF = 9). The quality flag QF = 9 can be considered as secure since the MUSE spectral resolution allows us to distinguish the shape or doublet nature of narrow emission lines (e.g. Lyman-α and [OII]). In a second step, we performed a blind search in the MUSE data cube for emission lines that are not associated with a photometric detection. For instance, many Lyman-α emitters have no optical or near-infrared photometric counterpart (see e.g. de La Vieuville et al. 2019; Wisotzki et al. 2018; Claeyssens et al. 2022; Thai et al. 2023). This search is done using a combination of automatic detection on narrow-band images built from the data cube

and a visual inspection. In total, 17 emitters (mainly Lyman-α) are detected in this step.

The full spectroscopic sample contains 107 reliable (i.e. likely or secure, QF $\geq$ 2) redshift measurements of extragalactic objects, two are foreground ($z < 0.324$) objects, 58 are at the cluster redshift ($0.324 < z < 0.349$; see Sect. 3.1), including 50 cluster member galaxies, 47 redshift measurements are in the cluster background ($z > 0.349$; see Sect. 3.2), out of which we identify 13 lensed multiple images from four background emitters. The redshift catalogue is summarised in Table A.1.

3.1. Cluster galaxies

The cluster MACS0138 is clearly visible in the distribution of the redshift measurements included in Table A.1 as an overdensity around the redshift range of $0.32 \lesssim z \lesssim 0.35$. We identify the spectroscopic cluster members by selecting all galaxies with a reliable redshift estimate (i.e. with a QF $\geq$ 2) and a rest-frame relative line-of-sight velocity within $\Delta V = 2500\,\mathrm{km\,s^{-1}}$ with respect to the cluster mean line-of-sight velocity, determined from the width of the redshift space cluster member distribution, which corresponds to the redshift range $z = 0.324 - 0.349$. As clear from Fig. 2, the redshift distribution is well centred around $z_{\mathrm{cluster}} = 0.336$. Our catalogue contains 58 reliable redshift measurements in the relevant redshift range. This spectroscopic sample was used by Ertl et al. (in prep.), Suyu et al. (in prep.), and Acebron et al. (in prep.) as a basis for the catalogue of cluster members included within the strong lensing models presented therein. They excluded eight non-galactic objects from the catalogue, typically star forming clumps, marked in Table A.1 with an asterisk, for a final catalogue comprising 50 spectroscopically confirmed cluster members. A visual spectral study of the 50 cluster members reveals that the vast majority of the sample (45 members), as expected, shows spectra typical of old, passively evolving stellar populations. This includes the brightest cluster galaxy (BCG), whose spectrum is strongly contaminated by broad emission lines, presumably from its active galactic nucleus (AGN). The remaining five cluster members are active (mostly blue or jellyfish galaxies). In Sect. 4, we use the MUSE spectra to probe the stellar kinematics of the brightest red members, in order to obtain a prior on their total mass structure. The cluster member catalogue was completed in Ertl et al. (in prep.) with the addition of non-spectroscopic members selected on the basis of the colour-magnitude and colour-colour relations of the cluster.

3.2. Background objects and multiple image systems

The catalogue contains 47 redshift measurements with $z > 0.349$, from 38 individual background emitters, when accounting for multiple images of the same sources. The redshift space distribution shows a secondary peak at $z \approx 0.37$, visible in Fig. 2, possibly from a smaller group of galaxies in the background. Their impact on the strong lensing model is accounted for in Ertl et al. (in prep.), Suyu et al. (in prep.), and Acebron et al. (in prep.). The catalogue contains four lensed images of the host of SN Encore and SN Requiem, at $z = 1.95$, confirmed from the MgII absorption doublet. A fifth image was identified in Ertl et al. (in prep.), blended with the BCG light. Besides the three multiple images from an [OII] emitter which was previously reported in Rodney et al. (2021), we were able to identify two further lensed background sources at redshifts $z = 3.152$ and $z = 3.420$, for a total of 13 lensed multiple images with a reliable redshift measurement (i.e. QF$\geq$ 2), which we mark in bold

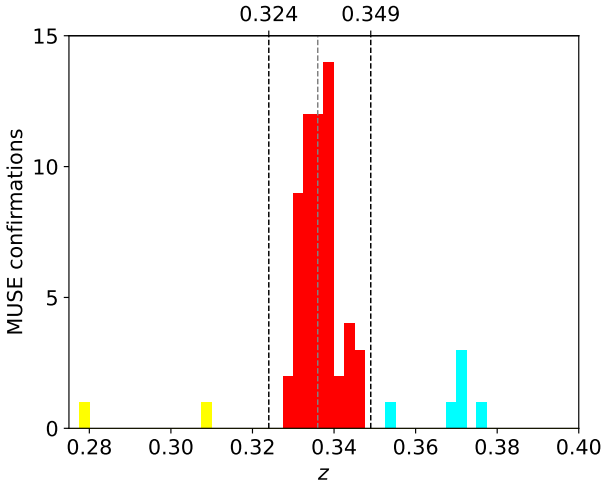


Fig. 2: The histogram shows the redshift distribution around the cluster redshift ($z_{\mathrm{cluster}} = 0.336$, marked with a grey dashed line). Cluster members are indicated in red, while foreground and background objects are marked in yellow and cyan, respectively. The vertical lines indicate the region with a relative velocity of ± 2500 km s^{-1} from the cluster mean redshift.

in Table A.1. The search was performed both from our spectroscopic catalogue and through a blind search for simultaneously appearing spectral features when scanning the MUSE data cube. Our multiple image catalogue was used as the basis for the new SL models. Specifically, we identify multiple lensed images of a star-forming galaxy and two high-z Lyman-α emitters. The first source is at $z = 0.767$, with prominent [OII] and [OIII] emission lines, including a faint image appearing close to the centre of the BCG. Owing to its clumpy nature, two components of the source have been identified in Ertl et al. (in prep.) and their multiple images have been used as separate constraints for the SL model (System 4). The two Lyman-α sources are at $z = 3.152$ and 3.420 and were identified from scanning the MUSE cube, as they lack a clear photometric counterpart in *HST* and *JWST* data. They are included in the SL model by Ertl et al. (in prep.) as Systems 5 and 6. The position of the emission line sources can also be inferred on the basis of the MUSE surface brightness at the corresponding wavelength, which we show in Fig. 3 for the newly identified lensed systems. In Fig. 4, instead, we show the MUSE spectra of the secure (QF = 3), marking the spectral emission or absorption features used for their identification and confirmation. Finally, we identify an arc-like region ($\mathrm{ID_{MUSE}}$=1755) lensed by a cluster member ($\mathrm{ID_{MUSE}}$=1631). We extracted its spectrum from an arc-shaped aperture, to avoid contamination from the nearby member, and measured a likely (QF=2) redshift $z = 1.945$. Given that its value is not secure, the redshift is not used as a constraint in the 'gold' sample of lensed images for SL models.

4. Stellar kinematics of galaxies

The depth of the available MUSE data allows for an accurate study of the line-of-sight stellar kinematics of several member and line-of-sight galaxies, providing us with a further tracer of their total mass distribution, which has been used in Ertl et al. (in prep.) to enhance the accuracy of the description of the galaxy-scale mass components within the strong lensing models of MACS0138. In this section, we briefly describe the pipeline

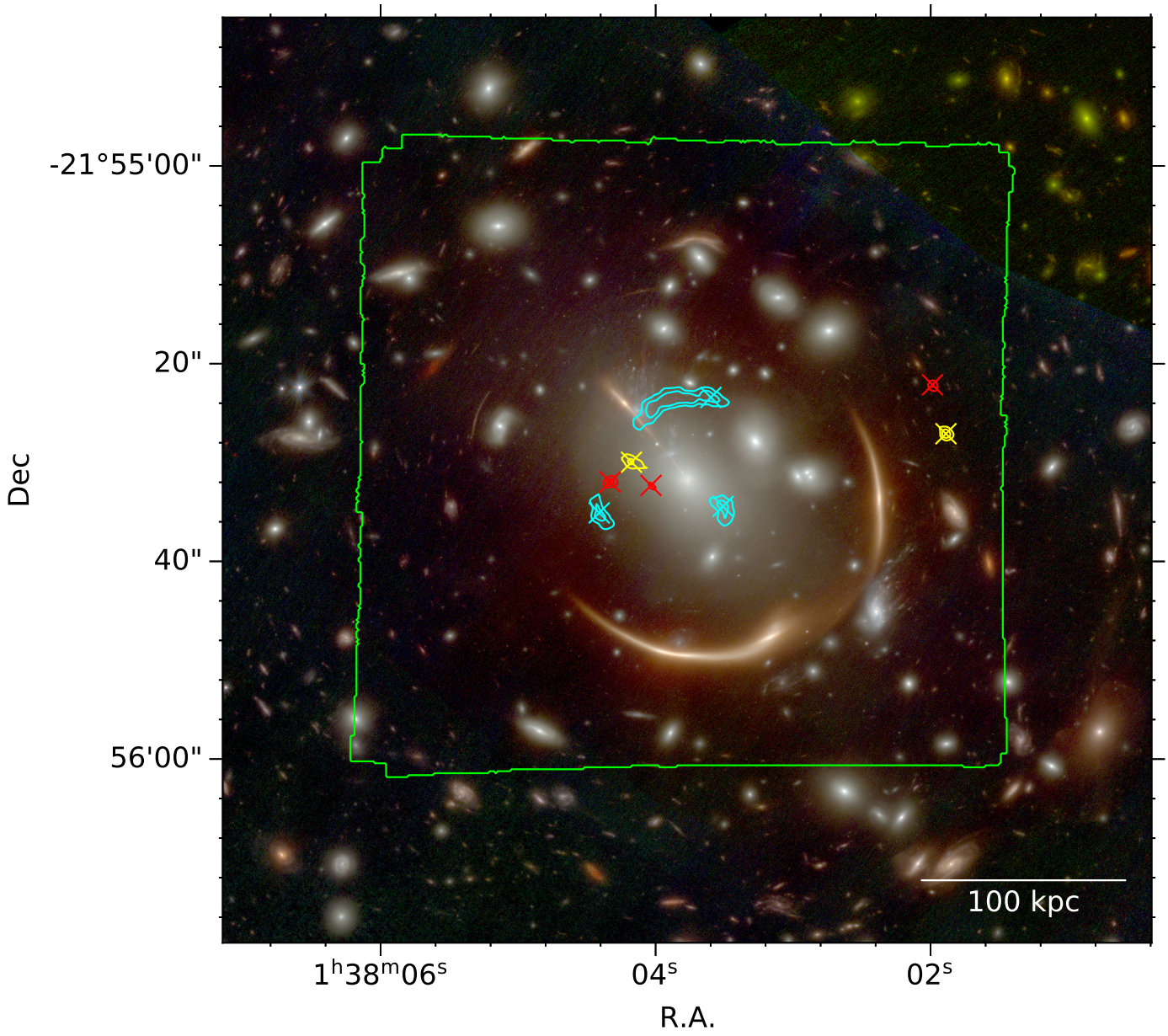


Fig. 3: MUSE FoV on MACS0138 overlaid on a colour image built from the *JWST* NIRCam images (the bands used are the same as in Fig. 1). The cyan, red and yellow lines show iso-surface-brightness contours for the MUSE cube at the wavelengths of the emission lines used to detect the three lensed sources: [OII] emission at $z = 0.767$ (in cyan), Lyman-α emission at $z = 3.152$ (in red) and Lyman-α emission at $z = 3.420$ (in yellow). The two Lyman-α emissions are newly discovered sources strongly lensed by this cluster. We mark the position of the secure multiply-lensed images detections (QF = 3) for the three sources (Systems 4, 5 and 6, respectively) with a cross.

for the spectral measurement of the line-of-sight stellar velocity dispersion of the bright galaxies falling within the MUSE FoV, detailed in Granata et al. (in prep.), and present the kinematic catalogue adopted by Ertl et al. (in prep.). Finally, we present some insights on the total mass structure of the cluster members obtained enhancing strong lensing modelling with priors from stellar kinematics.

4.1. Measured velocity dispersions from MUSE spectroscopy

We measured the value of the line-of-sight stellar velocity dispersion, σ_v, of each galaxy included in the analysis following the procedure presented in Granata et al. (2023) and Granata et al. (in prep.). For the kinematic analysis, we used the public spectral fitting code `pPXF`* (penalized pixel-fitting, Cappellari & Emsellem 2004; Cappellari 2017, 2023) to perform a full-spectrum fit of the continuum and of the absorption lines of the observed spectra in the rest-frame wavelength range [3700 – 5100] Å. The optimisation fits simultaneously for the stellar population and for the line-of-sight stellar velocity distribution of the observed galaxy, by comparing its spectrum with a combination of stellar templates chosen from a set of high-resolution UVB stellar spectra from the X-shooter Spectral Library (XSL) DR3 (Verro et al. 2022), convolved with a line-of-sight velocity distri-

*Version 8.2.6

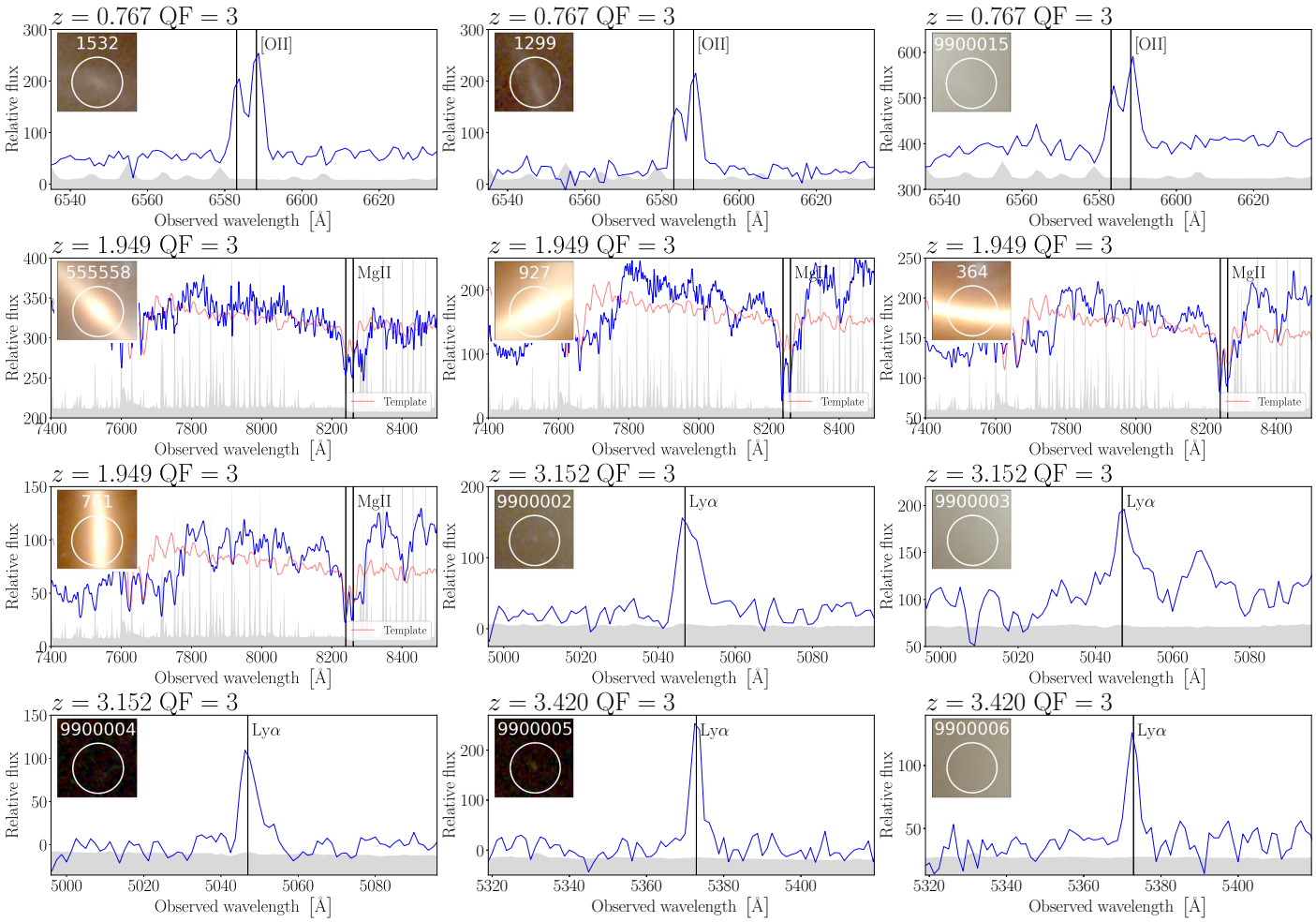


Fig. 4: Spectra of the secure (QF = 3) multiple images included in our catalogue. The vertical line indicates the observed position of the main spectral feature used for the identification ([OII], MgII, and Lyman-α). We show the re-scaled variance in gray. The measured redshift and its quality flag are indicated in each figure title. The *HST* cutouts are 2″ on each side, and show the $\mathrm{ID_{MUSE}}$ of the object in Table A.1.

bution. We based our template selection on the work of Knabel et al. (2025), who showed that template selection is the main source of systematics for stellar kinematic studies of early-type galaxies. They examined all 830 XSL DR3 spectra and purged those that are not flux calibrated or corrected for slit loss or extinction. They then visually inspected all remaining templates, flagging any potential issue with them (e.g. problems with extinction or telluric corrections, high noise, or emission lines) and the wavelength range affected. The authors kindly provided us with the list of clean templates and with wavelength flags for possible problems affecting them, allowing us to compile a final library of 462 templates which we use for our kinematic studies.

We combined the templates with 12-th degree additive Fourier polynomials, and we chose a Gaussian line-of-sight velocity distribution, as we are interested in fitting only its first two moments. We checked the robustness of the fit with respect to the choice of the stellar template library, and, as done in Cappellari & Emsellem (2004), we verified its reliability with a set of 16,000 simulated MUSE spectra of cluster members, reproducing a variety of spectral type and observing conditions (Granata et al. in prep.). We found that a spectral $S/N \geq 10$ is required to guarantee consistently accurate velocity dispersion measurements. Here and in the continuation of this paper we use the notation S/N to refer to the average signal-to-noise ratio of the MUSE wavelength bins that we consider for the velocity dispersion fit. Given the spectral sampling of 1.25 Å of MUSE, a signal-to-noise per bin of $S/N = 10$ corresponds to a signal-to-noise per angstrom of 8 $\mathrm{Å}^{-1}$. These simulations were also used to obtain a reliable estimate of the error on the value of σ_v. On one hand, `pPXF` provides a formal uncertainty on the value of σ_v, from the covariance matrix of the errors on the fitted parameters, which we re-scaled assuming that the best-fit χ^2 matches the number of degrees of freedom in the fit. Whilst this method can provide an order-of-magnitude estimate of the uncertainty assuming the fit is good, it can significantly under-estimate the uncertainty in the case of noisier spectra or low values of σ_v (Cappellari & Emsellem 2004). In this regime, simulations can yield a more reliable estimate of the accuracy of the recovered values (Cappellari & Emsellem 2004): in Granata et al. (in prep.) we probe the relative uncertainty on the value of sigma as a function of S/N from the 1σ scatter of the recovered σ_v values about the input velocity dispersion of the 16,000 simulated spectra. Similarly to Bergamini et al. (2019), Granata et al. (in prep.) fitted a relation between the relative uncertainty on σ_v and S/N, which we used here to obtain a more reliable estimate of the error associated with the spectral noise of the recovered σ_v value. We chose, conservatively, to sum in quadrature this estimate of

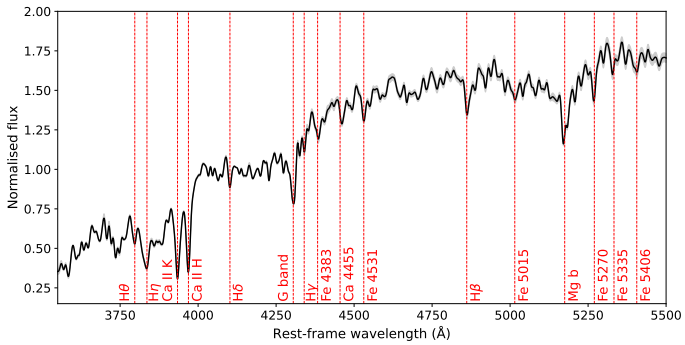


Fig. 5: VLT/MUSE mean stacked spectrum of the 13 cluster members, all except the BCG, for which we have obtained a line-of-sight stellar velocity dispersion measurement. The shaded region shows the standard deviation of each spectral pixel. The spectra are smoothed by applying a Gaussian kernel with a standard deviation of 3.75 Å. The red dashed vertical lines indicate the main absorption features of the spectrum.

the error on σ_v with the formal parametric error given by pPXF to obtain our final uncertainty estimates, reported in Table 1.

As shown in Granata et al. (in prep.), we can increase the S/N of the spectra, thus extending the sample of cluster members for which we can probe the stellar kinematics, by weighting the MUSE cube with the members' surface brightness. To this purpose, we used the *HST* F814W band image, de-graded and re-binned to the PSF and pixel-scale of our MUSE observations, and extracted the spectra from large circular apertures with a 1.5″ radius, centred on the galaxy centre of light. The spectra resulting from the weighted average are representative of the central regions of the members, which are sampled with a higher weight due to their higher surface brightness: the velocity dispersion value obtained from them are on average equivalent to those measured within the galaxy half-light radius. We can thus probe the central velocity dispersion of the cluster galaxies with high S/N and without the need for aperture corrections. In Fig. 5, we show a VLT/MUSE mean stacked spectrum of the 13 early-type cluster member galaxies (excluding the BCG) for which we have obtained a velocity dispersion measurement. The stacked spectrum, obtained from a sum of the spectra of the 13 members normalised using their median flux value in the rest-frame 4125–4275 Å wavelength range, was smoothed with a Gaussian kernel with a standard deviation of 3.75 Å, thus highlighting the spectral features more clearly. The shaded area shows the uncertainty obtained from the standard deviation scatter of the 13 spectra about the mean in each spectral bin. The stacked spectrum is typical of an old, passively evolving, stellar population, and clearly showcases several absorption features, such as the Ca II H and K, the G-band, and the Hβ lines, whose width can be used to anchor the fit of the line-of-sight stellar velocity dispersion of the members.

In Table 1, we present our catalogue of reliable velocity dispersion measurements, comprising 14 red cluster galaxies and two red line-of-sight background galaxies, while in Fig. B.1, we showcase the fits of their spectra performed with pPXF. Given the large apertures used for the spectrum extraction, we visually checked all spectra to avoid contamination from any nearby object, excluding all instances of contaminated or blended spectra, which are frequent in the most crowded regions of the cluster, besides all spectra with $S/N < 10$. The spectrum of the BCG clearly shows several prominent gas emission lines (see Fig. B.1). We find that the lowest contamination is obtained extracting the spectrum within a small circular aperture (with a 0.6″ radius) from the BCG centre of light, avoiding the light-weighting procedure. Given that the observed emission lines influence some of the stellar absorption features used for our stellar kinematic studies, we masked out all the spectral regions within the wavelength range considered potentially affected by them, and we imposed a conservative 5% uncertainty on the BCG stellar velocity dispersion value, as reported in Table 1, where the BCG is marked with an asterisk. As discussed, the total uncertainty $\delta\sigma_v$ on the velocity dispersion value is obtained as the quadrature sum between the uncertainty provided by pPXF as a result of the spectral fit and the uncertainty associated to the S/N.

4.2. The Faber-Jackson relation for the cluster members

The total mass distribution of member galaxies in cluster-scale lensing models is typically parametrised by a truncated dual pseudo-isothermal elliptical mass distribution (dPIE; Elíasdóttir et al. 2007; Suyu & Halkola 2010) with vanishing core radius. Their total mass distribution thus only depends on two parameters: the velocity dispersion σ_v, and the truncation (or half-mass) radius r_t. Cluster-scale strong lensing events produce most frequently multiple image systems with separations of the same order of magnitude as the cluster Einstein radius, typically higher than 10″. In these cases, the positions of the multiple images are not very sensitive to the details of the total mass distribution of the members. The velocity dispersion and the truncation radius of the cluster members are thus strongly degenerate (Bergamini et al. 2019), as the same galaxy total mass can be obtained with a higher (lower) velocity dispersion and a lower (higher) truncation radius, leading to a more (less) compact total mass distribution for the members. To reduce the number of free parameters during the model optimisation, allowing for a positive number of degrees of freedom, the two quantities are often linked to the observed total luminosity L of the members by calibrating power-law scaling relations.

As found by Faber & Jackson (1976), a power-law relation holds between the central stellar velocity dispersion of elliptical galaxies $\sigma_{v,0}$ and their total luminosity L in a given band. As shown by Bergamini et al. (2019), for a vanishing core radius, the velocity dispersion parameter of the dPIE profile is well approximated by the value of the central line-of-sight stellar velocity dispersion. As such, the calibrated Faber-Jackson relation can be used to obtain an observational prior on the corresponding scaling law used to link σ_v and L. As detailed in Sect. 4.1, we have accurate measurements of the central stellar velocity dispersion for 13 red cluster galaxies, excluding the BCG, which has a different morphology compared to other elliptical galaxies and is not necessarily well described by the same Faber-Jackson relation. Ertl et al. (in prep.) have measured the structural parameters of these objects in the *HST* band F160W. The total magnitude of the members in this band m_{F160W} is a good proxy of the total stellar mass of the members (Grillo et al. 2015). We choose the second brightest cluster member $\mathrm{ID_{MUSE}}$=1308 with $m_{\mathrm{F160W}} = 17.985$ as a reference, and write the velocity dispersion for the i-th cluster member with magnitude $m_{\mathrm{F160W},i}$ as

$$\sigma_{v,i} = \sigma_{v,\mathrm{ref}} \times 10^{0.4\,(17.985 - m_{\mathrm{F160W},i})\,\alpha}, \quad (1)$$

where $\sigma_{v,\mathrm{ref}}$ and α are parameters of the scaling relation that we will determine based on our data. We follow the procedure detailed in Bergamini et al. (2019) (Appendix B), and fit Eq.

Table 1: Catalogue of measured velocity dispersion values.

ID	ID_{MUSE}	R.A. (J2000)	Dec (J2000)	σ_v (km s^{-1})	$\delta\sigma_v$ (km s^{-1})	S/N
55	895	24.5162254	−21.9326011	114.7	4.4	22.4
58	930	24.5078679	−21.9329074	97.1	5.2	18.1
69	1032	24.5090052	−21.9312181	157.2	5.3	23.8
78	1127	24.5149459	−21.9276509	148.0	3.9	47.1
102	1210	24.5213768	−21.9239768	176.4	3.1	51.7
90	1211	24.5076178	−21.9271544	88.0	7.9	12.4
115	1308	24.5114284	−21.9213096	210.5	3.1	56.8
191	1386	24.5214401	−21.9183725	175.5	2.5	59.3
203	1433	24.5164250	−21.9212544	161.3	3.4	44.9
116	1457	24.5156388	−21.9227696	155.1	5.0	29.7
154	1498	24.5129692	−21.9203716	137.3	2.9	43.0
193	1631	24.5153499	−21.9192529	214.8	4.1	44.8
156	1633	24.5162417	−21.9200615	171.0	5.2	28.5
0*	827	24.5157373	−21.9254784	321.9	16.1	52.7
51	751	24.5201843	−21.9325380	141.6	3.7	44.7
82	873	24.5136363	−21.9244078	237.7	1.8	127.5

Notes. We identify the galaxies included in this catalogue with their photometric ID (first column, see Ertl et al. in prep.) and MUSE ID (ID_{MUSE} in the second column, see Table A.1). We report the measured stellar velocity dispersion value of the galaxy with σ_v (fifth column) and its uncertainty with $\delta\sigma_v$ (sixth column), and the spectral S/N (seventh column). We mark the BCG with an asterisk. The horizontal line separates cluster members from background galaxies.

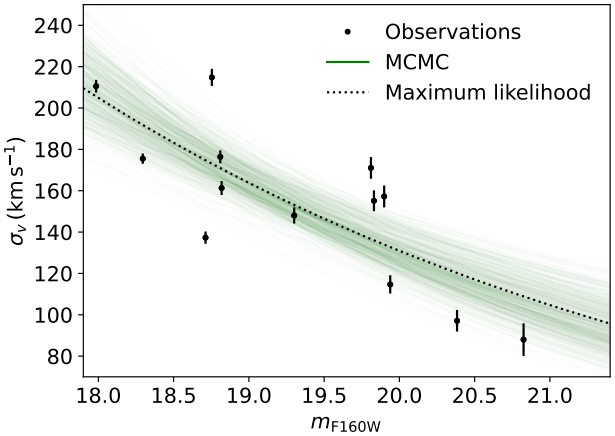


Fig. 6: Faber-Jackson relation for the members of MACS0138. The green lines represent 100 realisations randomly drawn from the posterior probability distribution of the scaling relation parameters, while the black dotted line shows the maximum-likelihood solution. The black dots are the 13 cluster members with an observed velocity dispersion used for the scaling law calibration.

(1) with affine-invariant Markov chain Monte Carlo (MCMC, Goodman & Weare 2010; Foreman-Mackey et al. 2013). We explore the posterior probability distribution for the values of $\sigma_{v,\mathrm{ref}}$ and α as defined in Eq. (1), and of the intrinsic scatter around the Faber-Jackson relation $\Delta\sigma_v$. The prior and likelihood functions, and the $\Delta\sigma_v$ are defined as in Eqs. (B.3) and (B.4) in Bergamini et al. (2019). The recovered value of $\sigma_{v,\mathrm{ref}}$ is compatible with the measured σ_v value for the reference galaxy (ID_{MUSE}=1308, see Table 1). In Fig. 6, we show the Faber-Jackson relation and its uncertainty, and the 13 cluster members used to optimise its parameters. These parameters are used in Ertl et al. (in prep.) to describe the cluster-member component in their SL model of

Table 2: Parameters of the Faber-Jackson relation for the members of MACS0138.

Parameter	Value
$\sigma_{v,\mathrm{ref}}$ (km s^{-1})	206^{+14}_{-13}
α	$0.25^{+0.05}_{-0.05}$
$\Delta\sigma_v$ (km s^{-1})	25^{+6}_{-4}

Notes. We show the median, 16th, and 84th percentile of the three optimised parameters, as defined in the main text.

MACS0138 more accurately. In Table 2, we report the median values, with a 1σ uncertainty, of the three optimised parameters, as a result of the posterior probability distribution exploration with MCMC.

We compare the Faber-Jackson relation found for MACS0138 with other SL galaxy clusters within the same redshift range, as calibrated by recent SL modelling in an effort to enhance the description of the cluster member total mass component. Specifically, we consider the massive clusters Abell 2744 (z=0.31, hereafter A2744, Bergamini et al. 2023a), Abell S1063 (z=0.35, hereafter AS1063, Bergamini et al. 2019; Mercurio et al. 2021), MACS J0416.1-2403 (z=0.40, hereafter MACS0416, Bergamini et al. 2023b), MACS J1206.2-0847 (z=0.44, hereafter MACS1206, Bergamini et al. 2019), SDSS J2222+2745 (z=0.49, hereafter SDSS2222, Acebron et al. 2022a), and SDSS J1029+2623 (z=0.59, hereafter SDSS1029, Acebron et al. 2022b). Looking at the slope α of the Faber-Jackson, defined in Eq. (1), we notice how most values agree with our findings, with a few exceptions. The kinematic studies previously listed find α values of 0.40, 0.27, 0.30, 0.27, 0.295, and 0.39 for A2744, AS1063, MACS0416, MACS1206, SDSS2222, and SDSS1029, respectively. These values are generally slightly higher, although compatible, with what we find, except for A2744 and SDSS1029, which show a steeper slope, less consistent with the proportionality between the total galaxy luminosity and σ_v^4 found by Faber & Jackson (1976). To perform a meaningful comparison, we consider the absolute

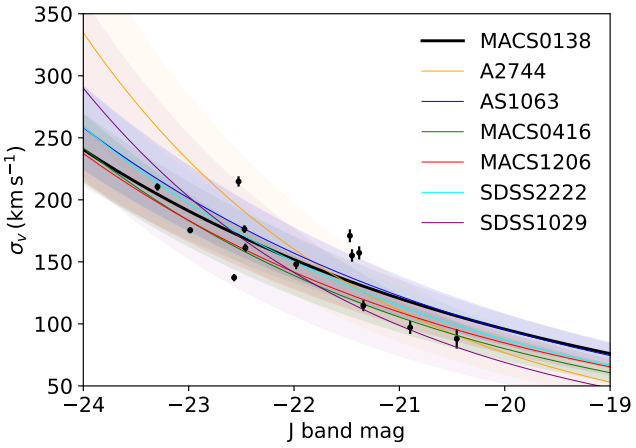


Fig. 7: Faber-Jackson relation for the members of MACS0138 compared with those for six SL clusters at $0.31 \leq z \leq 0.59$. We show the best-fit relation and its scatter for MACS0138 (in black), A2744 (in orange), AS1063 (in blue), MACS0416 (in green), MACS1206 (in red), SDSS2222 (in cyan), and SDSS1029 (in purple). The black dots are the 13 cluster members selected in Sect. 4.2.

magnitudes in the Two Micron All-Sky Survey (2MASS) J band. The conversion between the rest-frame J band and the observed-frame F160W band for all seven clusters was obtained with a K-correction based on a simulated early-type galaxy spectrum generated through the GALaxy EVolution (GALEV Kotulla et al. 2009) evolutionary synthesis models.

In Fig. 7, we show the measured values of σ_v for MACS0138 and the Faber-Jackson relations for MACS0138 and the six clusters listed above. The plot shows that all relations describe well our observed data-points within their scatter, even those with a significantly higher slope, which we find to be typically associated with a higher scatter about the relation. This suggests that we do not see statistically significant signs of evolution of the Faber-Jackson relation for early-type cluster members in the redshift range $0.31 \leq z \leq 0.59$, when considering total magnitude values in the same K-corrected rest-frame J band.

5. Summary

In this work, we presented a comprehensive spectroscopic analysis of the strong lensing galaxy cluster MACS0138, and an accurate study of the stellar kinematics of its bright cluster members. All our results are based on MUSE observations of the cluster core, including our recent 2.9 hours observations, for a total of approximately 3.7 hours of exposure time. In Table A.1, we release a catalogue of reliable spectroscopic redshifts (QF $\geq$ 2) containing 107 objects. Specifically, we identify 50 galaxy cluster members at $0.324 < z < 0.349$ and a small background group at $z \sim 0.37$. Our secure identification of the mass components along the line-of-sight is the basis for accurate SL modelling of the cluster, as shown by Ertl et al. (in prep.), Suyu et al. (in prep.), and Acebron et al. (in prep.). The catalogue also contains a lensed arc-like structure at $z = 1.945$ and 13 spectroscopically confirmed (QF $\geq$ 2) lensed multiple images from four background sources at $0.767 \leq z \leq 3.420$. Amongst these, we report four lensed images of the host of SN Encore and SN Requiem, and 11 images from three other lensed background sources, two of which are newly discovered here. Our new sample of multiply-lensed sources in a large redshift range provides accurate constraints on the cluster mass distribution in SL models, which will be necessary to obtain a reliable H_0 measurement from the observed SN time delays.

The depth of the MUSE data available has allowed us to accurately probe the stellar kinematics of several bright galaxies. In Table 1, we presented measured stellar velocity dispersion values for 14 cluster members and two background galaxies, separated by a horizontal line. These have been used as a prior for the description of the galaxy-scale mass components in the SL models presented in Ertl et al. (in prep.), Suyu et al. (in prep.), and Acebron et al. (in prep.), breaking the parametric degeneracy that typically affects SL models of clusters on these scales. We combined our σ_v measurements for 13 early-type cluster galaxies with their total magnitude in the *HST* F160W band, measured by Ertl et al. (in prep.), to calibrate the Faber-Jackson relation for the cluster members. We find a Faber-Jackson slope $\alpha = 0.25^{+0.05}_{-0.05}$, as defined in Eq. (1), and a scatter of 25^{+6}_{-4} km s^{-1} about the relation. We compare the Faber-Jackson relation calibrated for MACS0138 with six other SL clusters at $0.31 \leq z \leq 0.59$, finding compatible slope values, with two exceptions, and that all scaling laws seem to describe well our observed data-points within their scatter. When considering total magnitude values in the same K-corrected rest-frame J band, no clear evidence of an evolution of the relation with redshift is observed.

During the referee process for this paper, Flowers et al. (2024) published in a pre-print an independent spectroscopic redshift catalogue of MACS0138 and the calibration of the Faber-Jackson relation for its members. Their work differs from ours as they used shallower MUSE (i.e. 49 minutes from the ESO programme ID 0103.A-0777), leading to a smaller sample of 30 galaxies in the field with redshift measurements, including 23 cluster members, all of which are included in this work. In spite of the lower depth of the data, their velocity dispersion catalogue is instead slightly larger, comprising 19 objects, likely due to different selection cuts. Whilst we simultaneously fit for the stellar population and the velocity dispersion of each galaxy, the velocity dispersion measurements in Flowers et al. (2024) are performed with a single spectral template, built from a galaxy chosen amongst the brightest in the cluster. Flowers et al. (2024) test the impact of this and of other choices of modelling configuration on the velocity dispersion results, confirming its robustness. The Faber-Jackson relation is calibrated with respect to the magnitude measured in a bluer band (F555W instead of F160W), but the slope, normalisation, and scatter are consistent with our results, supporting the robustness of kinematic calibration of the Faber-Jackson relation. However, a few values reported in Flowers et al. (2024) differ very significantly from our measurements, such as the cluster member $\mathrm{ID_{MUSE}} = 930$ and the background galaxy $\mathrm{ID_{MUSE}} = 873$, for which they report velocity dispersion values of 167 ± 15 km s^{-1} and 291 ± 3 km s^{-1}, whilst we find 97 ± 5 km s^{-1} and 238 ± 2 km s^{-1}, respectively. A possible explanation for their significantly higher σ_v values is that their noisier spectra, owing to shallower observations, hinder the full recovery of the absorption line profile, as suggested by Fig. 7 in Flowers et al. (2024).

In conclusion, the new MUSE observations have paved the way for a deep analysis of the redshift-space distribution of cluster members and line-of-sight objects in the field of the cluster MACS0138, including the identification of multiply-lensed images of emission-line sources within a large redshift range. We have furthermore shown the importance of MUSE observations

for the study of the stellar kinematics of a sizeable sample of cluster and background galaxies. Our analysis will be key for the development of a set of accurate SL models of MACS0138, which is necessary to obtain a measurement of H_0 from the time delays between the multiple images of the lensed SN. The procedure and techniques presented in this work will prove extremely valuable in the upcoming years, as the Legacy Survey of Space and Time at the Vera C. Rubin Observatory will discover thousands of time-variable sources lensed by galaxies and clusters of galaxies (Oguri & Marshall 2010).

Acknowledgements. We thank Tommaso Treu and Shawn Knabel for the help and useful discussions on the velocity dispersion measurements. We thank Josè M. Diego and Conor Larison for their useful comments. GG and CG acknowledge support from the Italian Ministry of University and Research through grant PRIN-MIUR 2020SKSTHZ. SE and SHS thank the Max Planck Society for support through the Max Planck Fellowship for SHS. This work is supported in part by the Deutsche Forschungsgemeinschaft (DFG, German Research Foundation) under Germany's Excellence Strategy – EXC-2094 – 390783311. SS has received funding from the European Union's Horizon 2022 research and innovation programme under the Marie Skłodowska-Curie grant agreement No 101105167 — FASTIDIoUS. This project has received funding from the European Research Council (ERC) under the European Union's Horizon 2020 research and innovation programme (grant agreement No 771776). This work uses the following software packages: `Astropy` (Astropy Collaboration et al. 2013; Price-Whelan et al. 2018), `matplotlib` (Hunter 2007), `NumPy` (van der Walt et al. 2011; Harris et al. 2020), `pPXF` (Cappellari & Emsellem 2004; Cappellari 2023), `Python` (Van Rossum & Drake 2009), `Scipy` (Virtanen et al. 2020).

References

Acebron, A., Grillo, C., Bergamini, P., et al. 2022a, A&A, 668, A142
Acebron, A., Grillo, C., Bergamini, P., et al. 2022b, ApJ, 926, 86
Astropy Collaboration, Robitaille, T. P., Tollerud, E. J., et al. 2013, A&A, 558, A33
Bacon, R., Accardo, M., Adjali, L., et al. 2012, Msngr, 147, 4
Balestra, I., Mercurio, A., Sartoris, B., et al. 2016, ApJS, 224, 33
Beauchesne, B., Clément, B., Hibon, P., et al. 2024, MNRAS, 527, 3246
Bergamini, P., Acebron, A., Grillo, C., et al. 2023a, A&A, 670, A60
Bergamini, P., Grillo, C., Rosati, P., et al. 2023b, A&A, 674, A79
Bergamini, P., Rosati, P., Mercurio, A., et al. 2019, A&A, 631, A130
Caminha, G. B., Grillo, C., Rosati, P., et al. 2016, A&A, 587, A80
Caminha, G. B., Grillo, C., Rosati, P., et al. 2023, A&A, 678, A3
Caminha, G. B., Rosati, P., Grillo, C., et al. 2019, A&A, 632, A36
Cappellari, M. 2017, MNRAS, 466, 798
Cappellari, M. 2023, MNRAS, 526, 3273
Cappellari, M. & Emsellem, E. 2004, PASP, 116, 138
Claeyssens, A., Richard, J., Blaizot, J., et al. 2022, A&A, 666, A78
de La Vieuville, G., Bina, D., Pello, R., et al. 2019, A&A, 628, A3
Dhawan, S., Johansson, J., Goobar, A., et al. 2020, MNRAS, 491, 2639
Dhawan, S., Pierel, J. D. R., Gu, M., et al. 2024, MNRAS, 535, 2939
Efstathiou, G. 2020, arXiv e-prints, arXiv:2007.10716
Elíasdóttir, Á., Limousin, M., Richard, J., et al. 2007, arXiv e-prints, arXiv:0710.5636
Faber, S. M. & Jackson, R. E. 1976, ApJ, 204, 668
Flowers, A., O'Donnell, J. H., Jeltema, T. E., Wetzell, V., & Roberts, M. G. 2024, arXiv e-prints, arXiv:2412.19955
Foreman-Mackey, D., Hogg, D. W., Lang, D., & Goodman, J. 2013, PASP, 125, 306
Freedman, W. L., Madore, B. F., Jang, I. S., et al. 2024, arXiv e-prints, arXiv:2408.06153
Goodman, J. & Weare, J. 2010, Communications in Applied Mathematics and Computational Science, Vol. 5, No. 1, p. 65-80, 2010, 5, 65
Granata, G., Bergamini, P., Grillo, C., et al. 2023, A&A, 679, A124
Granata, G., Mercurio, A., Grillo, C., et al. 2022, A&A, 659, A24
Grillo, C., Karman, W., Suyu, S. H., et al. 2016, ApJ, 822, 78
Grillo, C., Rosati, P., Suyu, S. H., et al. 2018, ApJ, 860, 94
Grillo, C., Suyu, S. H., Rosati, P., et al. 2015, ApJ, 800, 38
Harris, C. R., Millman, K. J., van der Walt, S. J., et al. 2020, Nature, 585, 357–362
Huber, S. & Suyu, S. H. 2024, A&A, 692, A132
Hunter, J. D. 2007, Computing in Science & Engineering, 9, 90
Jauzac, M., Mahler, G., Edge, A. C., et al. 2019, MNRAS, 483, 3082
Kelly, P. L., Rodney, S., Treu, T., et al. 2023, Science, 380, abh1322
Knabel, S., Mozumdar, P., Shajib, A. J., et al. 2025, arXiv e-prints, arXiv:2502.16034
Kotulla, R., Fritze, U., Weilbacher, P., & Anders, P. 2009, MNRAS, 396, 462
Lagattuta, D. J., Richard, J., Bauer, F. E., et al. 2022, MNRAS, 514, 497
Meneghetti, M., Cui, W., Rasia, E., et al. 2023, A&A, 678, L2
Meneghetti, M., Davoli, G., Bergamini, P., et al. 2020, Science, 369, 1347
Meneghetti, M., Ragagnin, A., Borgani, S., et al. 2022, A&A, 668, A188
Mercurio, A., Rosati, P., Biviano, A., et al. 2021, A&A, 656, A147
Moresco, M., Amati, L., Amendola, L., et al. 2022, Living Reviews in Relativity, 25, 6
Natarajan, P. & Kneib, J.-P. 1997, MNRAS, 287, 833
Navarro, J. F., Frenk, C. S., & White, S. D. M. 1997, ApJ, 490, 493
Newman, A. B., Belli, S., Ellis, R. S., & Patel, S. G. 2018a, The Astrophysical Journal, 862, 125
Newman, A. B., Belli, S., Ellis, R. S., & Patel, S. G. 2018b, The Astrophysical Journal, 862, 126
Oguri, M. & Marshall, P. J. 2010, MNRAS, 405, 2579
Pierel, J. D. R., Frye, B. L., Pascale, M., et al. 2024a, ApJ, 967, 50
Pierel, J. D. R., Newman, A. B., Dhawan, S., et al. 2024b, ApJ, 967, L37
Planck Collaboration. 2020, A&A, 641, A6
Price-Whelan, A. M., Sipőcz, B. M., Günther, H. M., et al. 2018, AJ, 156, 123
Ragagnin, A., Meneghetti, M., Bassini, L., et al. 2022, A&A, 665, A16
Refsdal, S. 1964, MNRAS, 128, 307
Richard, J., Patricio, V., Martinez, J., et al. 2015, MNRAS, 446, L16
Riess, A. G., Anand, G. S., Yuan, W., et al. 2024, The Astrophysical Journal Letters, 962, L17
Riess, A. G., Scolnic, D., Anand, G. S., et al. 2024, arXiv e-prints, arXiv:2408.11770
Riess, A. G., Yuan, W., Macri, L. M., et al. 2022, The Astrophysical Journal Letters, 934, L7
Rodney, S. A., Brammer, G. B., Pierel, J. D., et al. 2021, Nature Astronomy 2021 5:11, 5, 1118
Soto, K. T., Lilly, S. J., Bacon, R., Richard, J., & Conseil, S. 2016, MNRAS, 458, 3210
Suyu, S. H. & Halkola, A. 2010, A&A, 524, A94
Thai, T. T., Tuan-Anh, P., Pello, R., et al. 2023, A&A, 678, A139
van der Walt, S., Colbert, S. C., & Varoquaux, G. 2011, Computing in Science Engineering, 13, 22
Van Rossum, G. & Drake, F. L. 2009, Python 3 Reference Manual (Scotts Valley, CA: CreateSpace)
Verro, K., Trager, S. C., Peletier, R. F., et al. 2022, A&A, 660, A34
Virtanen, P., Gommers, R., Oliphant, T. E., et al. 2020, Nature Methods, 17, 261
Weilbacher, P. M., Palsa, R., Streicher, O., et al. 2020, A&A, 641, A28
Wisotzki, L., Bacon, R., Brinchmann, J., et al. 2018, Nature, 562, 229
Wojtak, R. & Hjorth, J. 2022, MNRAS, 515, 2790
Wojtak, R. & Hjorth, J. 2024, MNRAS, 533, 2319

Appendix A: MUSE spectroscopic redshift catalogue.

In this Appendix, we present the final MUSE spectroscopic redshift catalogue, containing 107 reliable (i.e. likely or secure QF $\geq$ 2) redshift measurements of extragalactic objects, with two sources in the foreground, 58 at the cluster redshift, including 50 cluster galaxies, and 47 in the cluster background, as discussed in Sect. 3.

Table A.1: MUSE spectroscopic redshift catalogue.

ID	ID_{MUSE}	R.A. (J2000)	Dec (J2000)	z	QF
–	9900008	24.5229109	−21.9260049	0.2789	9
–	555552	24.5159631	−21.9300671	0.3092	3
117	1738	24.5204485	−21.9197347	0.3285	3
–	1716*	24.5232187	−21.9209395	0.3291	3
320	1162	24.5178425	−21.9303273	0.3307	2
–	10002	24.5161968	−21.9247577	0.3307	3
–	10001	24.5172345	−21.9235510	0.3311	3
78	1127	24.5149459	−21.9276509	0.3316	3
–	1619*	24.5175558	−21.9223099	0.3317	3
–	555559*	24.5171543	−21.9208968	0.3318	3
–	1686*	24.5148629	−21.9213703	0.3318	3
103	1073	24.512084	−21.9252872	0.3323	3
–	1644*	24.516643	−21.9222194	0.3324	3
261	5555521	24.5097565	−21.9302674	0.3328	3
154	1498	24.5129692	−21.9203716	0.3329	3
262	1218	24.5130061	−21.9278434	0.3331	3
92	1304	24.5123572	−21.9253942	0.3332	3
199	1782	24.5099978	−21.9190911	0.3335	3
60	997	24.5153411	−21.9329004	0.3336	2
115	1308	24.5114284	−21.9213096	0.3337	3
76	1149	24.5228962	−21.9298747	0.3338	3
–	774	24.5099894	−21.9291747	0.3339	3
142	1551	24.5143184	−21.9224156	0.3341	3
–	1316*	24.5090635	−21.9274273	0.3345	3
–	1318*	24.5089117	−21.9274546	0.3348	3
70	1094	24.5119004	−21.930871	0.3352	3
55	895	24.5162254	−21.9326011	0.3353	3
85	1256	24.510652	−21.9279027	0.3357	3
113	1475	24.5150361	−21.9242069	0.3360	2
135	1535	24.5133605	−21.9225114	0.3360	3
485	2000	24.51663	−21.9244886	0.3363	3
129	1513	24.5201735	−21.9229667	0.3365	3
93	555553	24.5141805	−21.927675	0.3368	2
267	1642	24.5128585	−21.9217549	0.3370	2
116	1457	24.5156388	−21.9227696	0.3372	3
90	1211	24.5076178	−21.9271544	0.3372	3
105	555554	24.5108496	−21.9255751	0.3374	3
102	1210	24.5213768	−21.9239768	0.3379	3
153	1630	24.5241351	−21.919833	0.3379	3
106	5555536	24.5119913	−21.9254078	0.3380	3
0	827	24.5157373	−21.9254784	0.3381	3
58	930	24.5078679	−21.9329074	0.3383	3
63	1049	24.5207142	−21.9319295	0.3383	3
72	1147	24.5113797	−21.9300727	0.3385	3
193	1631	24.5153499	−21.9192529	0.3386	3
191	1386	24.5214401	−21.9183725	0.3386	3
265	1783	24.5222923	−21.9191665	0.3387	2
77	555551	24.5177768	−21.9292971	0.3390	3
69	1032	24.5090052	−21.9312181	0.3392	3
264	1582	24.5244402	−21.9220557	0.3394	2
156	1633	24.5162417	−21.9200615	0.3399	3
65	1003	24.5059888	−21.9311714	0.3406	3
52	898	24.5257606	−21.932203	0.3416	3
192	1701	24.5186628	−21.9198871	0.3427	3
202	1549	24.5233304	−21.9219431	0.3431	3
203	1433	24.516425	−21.9212544	0.3436	3
–	1431*	24.5084096	−21.9253918	0.3437	3
263	1543	24.5188906	−21.9228596	0.3453	3
266	1595	24.515279	−21.9220368	0.3463	3

Table A.1: Continued. MUSE spectroscopic redshift catalogue.

ID	ID_{MUSE}	R.A. (J2000)	Dec (J2000)	z	QF
189	1869	24.5140145	−21.917715	0.3472	3
–	1952	24.5166145	−21.9171875	0.354	9
67	1066	24.5171971	−21.9320865	0.370	3
82	873	24.5136363	−21.9244078	0.371	3
51	751	24.5201843	−21.932538	0.372	3
–	1070	24.5127061	−21.9320308	0.372	3
194	1608	24.5244187	−21.9196872	0.376	3
–	5555516	24.5132654	−21.9305945	0.459	3
–	9900014	24.5246215	−21.9324916	0.522	3
–	1838	24.5099019	−21.9183388	0.541	3
–	1911	24.5084136	−21.9176089	0.602	3
–	9900011	24.5103473	−21.9294554	0.652	3
–	**1532**	24.5150086	−21.923182	0.767	3
–	**9900015**	24.5146393	−21.9262452	0.767	3
–	**1299**	24.518391	−21.9264267	0.767	3
187	1674	24.5103495	−21.9164811	0.791	3
–	1826	24.5088558	−21.9189801	0.793	3
–	1897	24.5075894	−21.9178839	0.830	3
84	1200	24.5076133	−21.9264195	0.830	3
–	1436	24.50895	−21.9250223	0.862	3
–	1915	24.5085166	−21.9174518	0.870	3
–	1863	24.5163104	−21.9182446	0.951	3
183	1917	24.5205768	−21.9161932	0.952	3
–	1117	24.5133754	−21.931416	1.024	3
319	1093	24.5128482	−21.931183	1.024	3
–	1026	24.5189773	−21.9332474	1.347	3
–	1005	24.5188692	−21.9332751	1.347	3
205	1683	24.508369	−21.9205608	1.666	3
97	1332	24.5228653	−21.9262572	1.759	3
–	1755	24.5153988	−21.9187909	1.945	2
–	**555558**	24.5176138	−21.9233427	1.949	3
–	**927**	24.5132561	−21.9299314	1.949	3
–	**364**	24.5160096	−21.9303706	1.949	3
–	**761**	24.5099201	−21.9260449	1.949	3
–	1366	24.5255739	−21.9265684	2.950	2
–	**9900003**	24.5168229	−21.9256552	3.152	3
–	**9900002**	24.5180612	−21.9255557	3.152	3
–	**9900004**	24.5082954	−21.9228268	3.152	3
–	9900001	24.5209073	−21.9318334	3.361	9
–	**9900005**	24.507886	−21.9242017	3.420	3
–	**9900006**	24.5174131	−21.9250015	3.420	3
–	**9900007**	24.5158357	−21.9247664	3.420	2
–	9900009	24.5241269	−21.9286028	3.584	9
–	9900010	24.5226685	−21.9224566	3.620	3
–	9900012	24.5118702	−21.9177915	4.068	3
–	1175	24.5237221	−21.9302823	4.354	2
–	9900013	24.5238134	−21.9247531	4.641	3
–	1947	24.5175665	-21.9173905	6.353	3

Notes. We identify the sources included in this catalogue with their photometric ID (see Ertl et al. 2024) and ID_{MUSE}. We report the right ascension, declination, spectroscopic redshift z, and the corresponding uncertainty in terms of a quality flag QF, with 3 as secure, 2 as likely, and 9 as secure (based on a single emission line). The horizontal line separates objects at the cluster redshift from line-of-sight foreground and background galaxies. We mark the 13 lensed multiple images with a reliable redshift measurements (i.e. QF≥ 2) included in this catalogue with a bold-face ID, and the objects belonging to the cluster which are not galaxies with an asterisk (such non-galaxy objects are, e.g., star-forming clumps of jellyfish galaxies at the cluster redshift). They have been excluded from the cluster member sample used by Ertl et al. (in prep.), Suyu et al. (in prep.), and Acebron et al. (in prep.) to build SL models of the cluster.

Appendix B: Measuring velocity dispersions from MUSE spectra: spectral template fitting results

In this Appendix, we show the results of the pPXF-based line-of-sight stellar velocity dispersion fitting for 14 cluster members of MACS0138 and two background galaxies from their MUSE spectra. The procedure for these measurement is detailed in Sect. 4 and the results are presented in Table 1.

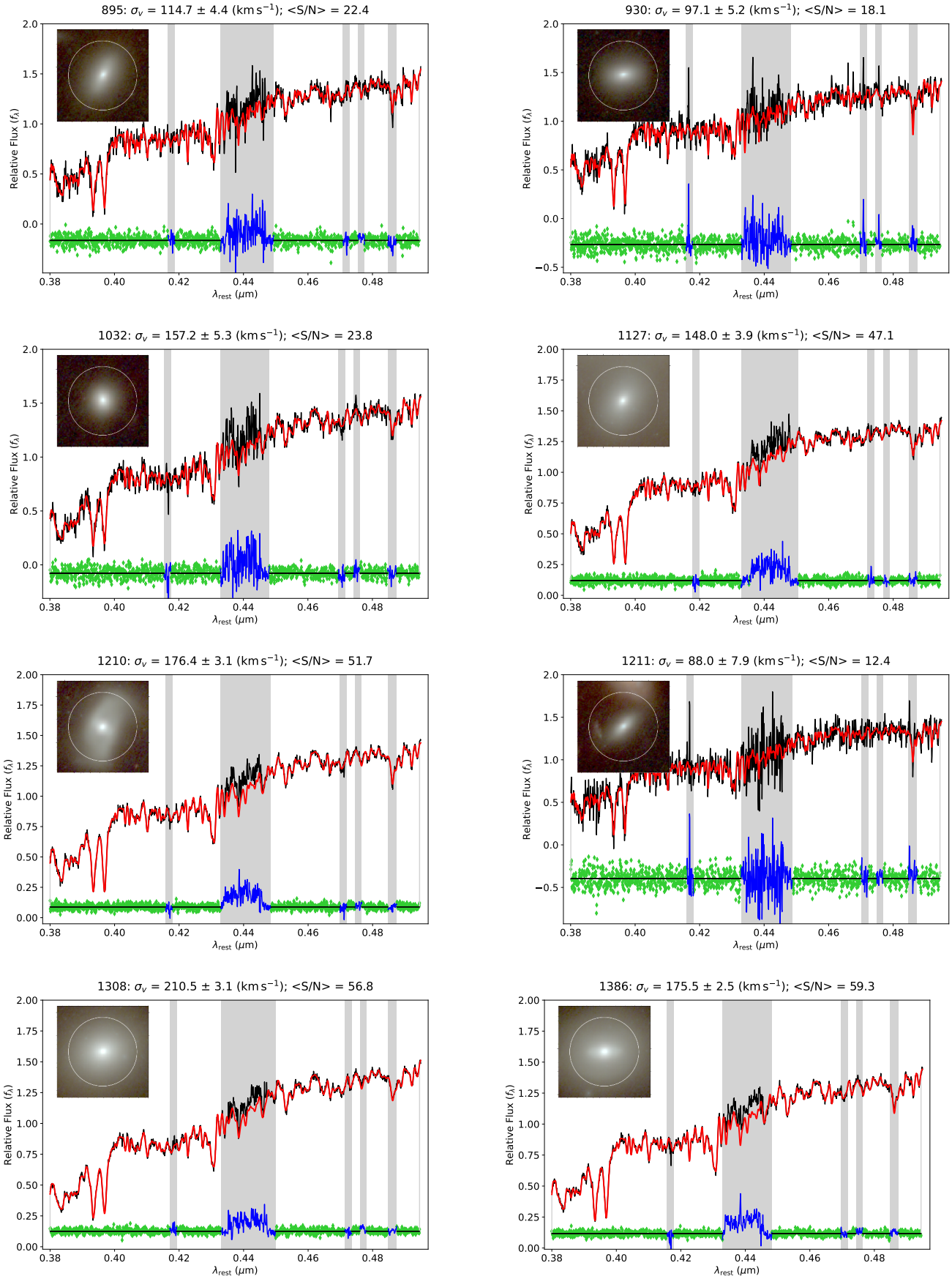


Fig. B.1: Stellar velocity dispersion fitting with pPXF. Observed MUSE spectra are in black, while the red curves are the pPXF best-fit models. The residuals of the data with respect to the model are shown in green. The regions masked, to avoid the impact of emission lines or of the subtraction of sky, laser, or telluric lines, are shaded in grey. The data−model residuals in these regions are marked in blue. In the top-left corner, we show a *JWST* RGB cutout of the object, 4″ on each side, and show the apertures used for the spectral extraction from the weighted MUSE cube. Measured σ_v and S/N values are shown above the plot.

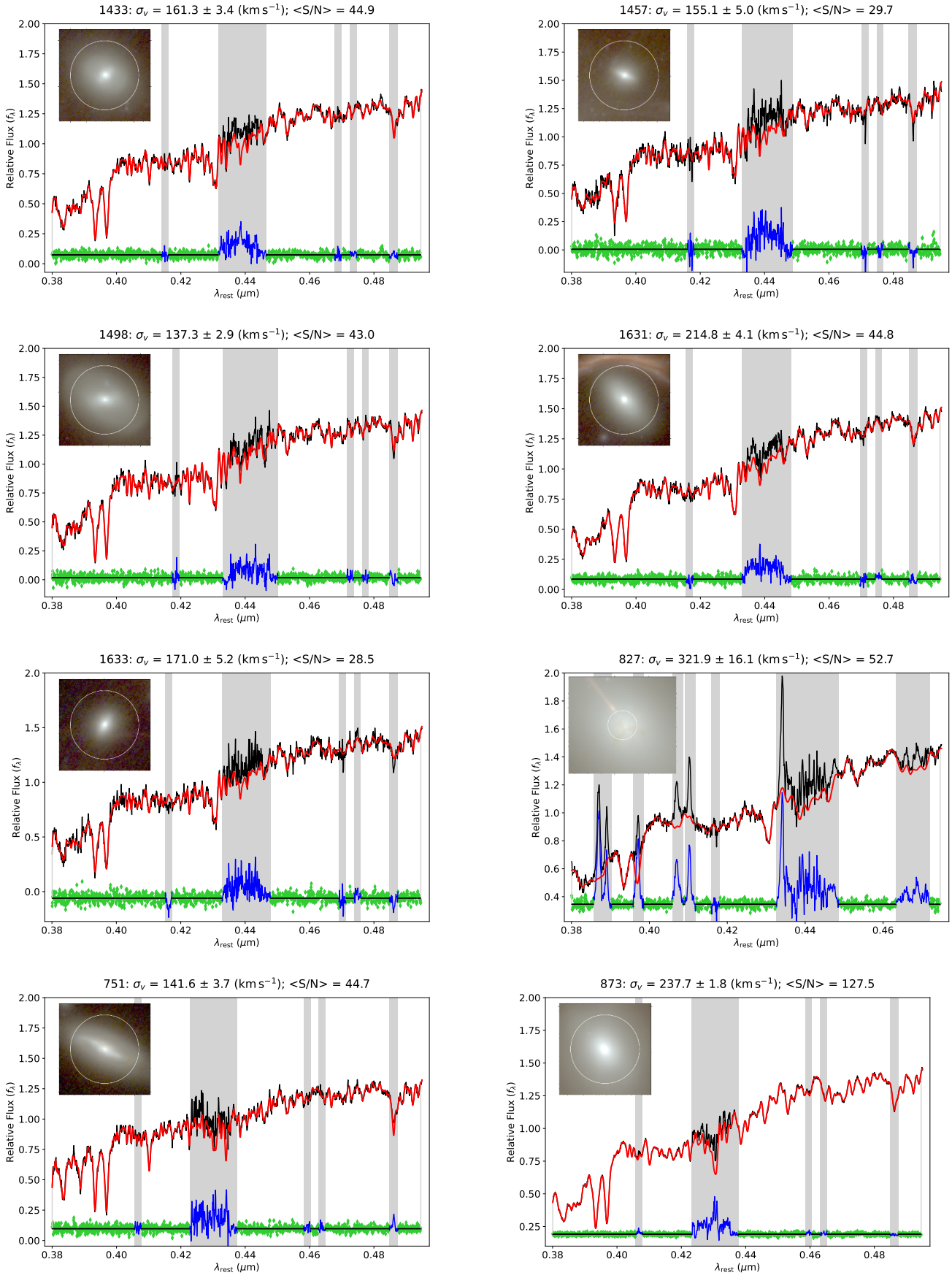


Fig. B.1 (continued): Velocity dispersion fitting with pPXF.